Subglacial topography and ice flux along the English Coast of Palmer Land, Antarctic Peninsula

Kate Winter[1], Emily A. Hill[1], G. Hilmar Gudmundsson[1], John Woodward[1]

[1]Department of Geography and Environmental Sciences, Faculty of Engineering and Environment, Northumbria University, Newcastle upon Tyne, UK

Correspondence to: Kate Winter (k.winter@northumbria.ac.uk)

Abstract. Recent satellite data have revealed widespread grounding line retreat, glacier thinning, and associated mass loss along the Bellingshausen Sea sector, leading to increased concern for the stability of this region of Antarctica. While satellites have greatly improved our understanding of surface conditions, a lack of radio-echo sounding (RES) data in this region has restricted our analysis of subglacial topography, ice thickness and ice flux. In this paper we analyse 3,000 km of 150 MHz airborne RES data collected using the PASIN2 radar system (flown at 3 – 5 km line spacing) to investigate the subglacial controls on ice flow near to the grounding lines of Ers, Envisat, Cryosat, Grace, Sentinel, Lidke and Landsat ice streams as well as Hall and Nikitin glaciers. We find that each outlet is topographically controlled, and when ice thickness is combined with surface velocity data from MEaSUREs (Mouiginot et al., 2019), these outlets are found to discharge over 39.2 ± 0.79 Gt a^{-1} of ice to floating ice shelves and the Southern Ocean. Our RES measurements reveal that outlet flows are grounded more than 300 m below sea level, and that there is limited topographic support for inland grounding line re-stabilisation in a future retreating scenario, with several ice stream beds dipping inland at ~5 degrees per km. These data reinforce the importance of accurate bed topography to model and understand the controls on inland ice flow and grounding line position as well as overall mass balance / sea level change estimates. RES data described in this paper are available through the UK Polar Data Center: https://doi.org/10.5285/E07D62BF-D58C-4187-A019-59BE998939CC (Corr and Robinson, 2020).

Short summary

Satellite measurements of the English Coast in the Antarctic Peninsula reveal that glaciers are thinning and losing mass, but ice thickness data is required to assess these changes, in terms of ice flux, and sea level contribution. Our ice penetrating radar measurements reveal that low-elevation subglacial channels control fast-flowing ice streams, which release over 38 gigatons of ice per year to floating ice shelves. This topography could make ice flows susceptible to future instability.

1 Introduction

Remote sensing satellites have increased our awareness and understanding of ice flows in Antarctica since their inception. In western Palmer Land, on the Antarctic Peninsula, Earth observation satellites have recorded widespread grounding line retreat (Christie et al., 2016; Konrad et al., 2018) and surface lowering (attributed to glacier thinning) in the last two decades (Wouters et al., 2015; Hogg et al., 2017; Smith et al., 2020), as well as surface velocity increases and significant mass loss (e.g. McMillan et al., 2014; Wouters et al., 2015; Martín-Español et al., 2016; Hogg et al., 2017), where ice flows contribute ~0.16 mm a^{-1} to global mean sea level (Wouters et al., 2015). Regional mass losses of -56± 8 Gt per year between 2010 and 2014 (Wouters et al., 2015) exceed the magnitude of interannual variability predicted by surface mass balance models (van Wessem et al., 2014, 2016), suggesting that the English Coast of western Palmer Land is undergoing significant change. While satellites have greatly improved our understanding of surface conditions and changes across Antarctica in recent years, a lack of ice thickness and subglacial topographic measurements in western Palmer Land has restricted our analysis of the controls on ice flow, ice flux and grounding line stability along the English Coast (Minchew et al., 2018). As subglacial topography exerts a strong control over ice flow it is critical to collect and analyse ice penetrating radar (IPR) data close to the grounding line in understudied regions of Antarctica.

In this paper we present a new, freely available IPR dataset along the English Coast of western Palmer Land, where several outlet glaciers were named after Earth observation satellites in 2019, in deference to the critical role that satellites have played in measuring and monitoring the Antarctic Ice Sheet (Fig. 1). We combine this new geophysical dataset with satellite measurements of ice flow speeds from MEaSUREs (Mouginot et al., 2019) to provide an improved picture of the subglacial controls on ice flows draining the English Coast, and directly assess the improvements to our understanding of bed topography and ice flux in the region as a result of such high-resolution IPR datasets.

2 Location and previous work

The English Coast of western Palmer Land contains numerous outlet glaciers which flow at speeds of ~0.5 to 2.5 m per day (Mouginot et al., 2019), from accumulation areas in central Palmer Land, towards ice shelves in the Bellingshausen Sea sector of Antarctica (Fig.1). A map of surface ice flow speeds in Figure 1 shows how the recently named Ers, Envisat, Cryosat and Grace ice streams drain into the fast-flowing George VI Ice Shelf, where floating ice connects Palmer Land to Alexander Island. Further south, Sentinel Ice Stream passes the local grounding line to form a floating tongue, connected in part to the neighbouring George VI Ice Shelf. Moving south of George VI Ice Shelf, Hall Glacier, Nikitin Glacier and Lidke Ice Stream each flow into Stange Ice Shelf. Whilst these outlet flows have separate accumulation zones that border the large Evans Ice Stream catchment (which drains into the Weddell Sea, on the other side of the Antarctic Peninsula) (Fig.1), their distinct flow units converge along the English Coast, at the local grounding zone. At the southern extremity of the English Coast, Landsat Ice Stream flows close to the catchment-defined boundary between the Antarctic Peninsula and West Antarctica. Slow flowing, almost stagnant ice separates the two tributary flows of Landsat Ice Stream for much of its length (Mouginot et al., 2019).

71   Our understanding of the English Coast of western Palmer Land is driven by data accessibility. Fast ice flow, and
72   heavily crevassed surfaces have largely restricted in-situ data collection in this region. The first Antarctic-wide
73   ice thickness and subglacial topography datasets: Bedmap (Lythe et al., 2001) and Bedmap2 (Fretwell et al., 2013)
74   relied on sparse IPR measurements for interpolation in this region of Antarctica. As a result, there are large
75   uncertainties in bed topography and ice thickness along the English Coast, which limit our understanding of
76   regional ice dynamics (Minchew et al., 2018). Inaccurate ice thickness and bed topography also hinder our ability
77   to assess the sensitivity of this region to future change using numerical ice flow models. Previous work has
78   therefore made use of more readily available satellite data, such as optical images, altimeter data and synthetic
79   aperture radar (SAR) measurements to assess regional change. Numerous studies have used these detailed datasets
80   to report on, and model recent changes in surface elevation and ice flow along the Bellingshausen Coast (e.g.
81   Pritchard et al., 2012; Christie et al., 2016; Hogg et al., 2017; Minchew et al., 2018), as well as Antarctica as a
82   whole (e.g. Helm et al., 2014; McMillan et al., 2014; Konrad et al., 2018; Smith et al., 2020). Collectively, this
83   work has highlighted a number of potential vulnerabilities in western Palmer Land. Recent mass loss of George
84   VI Ice Shelf and Stange Ice Shelf (totalling an estimated 11 Gt a^{-1}) (Rignot et al., 2019) raised concern that English
85   Coast outlet glaciers could be susceptible to the marine ice sheet instability mechanism (Wouters et al., 2015) -
86   where grounding-lines have a tendency to accelerate down a retrograde slope in the absence of compensating
87   forces (like buttressing ice shelves) (Schoof, 2007; Gudmundsson et al., 2012). These concerns are compounded
88   by recent changes in the grounded ice flows along the English Coast. Wouters et al. (2015) reported an average
89   surface lowering of ~ 0.5 m a^1 along the coastline between 2010-2014, whilst Hogg et al. (2017) calculated a 13%
90   increase in outlet glacier ice flow between 1993 and 2015. Importantly, if surface thinning and ice flow
91   acceleration across western Palmer Land continue in the future, dynamical imbalance could lead to further draw
92   down of the interior ice sheet (like it has done in other areas of Antarctica, (e.g. Shepherd et al., (2002); Rignot
93   (2008); Konrad et al. (2018)), leading to increased ice discharge into the ocean (Gudmundsson, 2013; Wouters et
94   al., 2015; Fürst et al., 2016; Kowal et al., 2016; Minchew et al., 2018), with resultant sea level rise. New, high-
95   resolution measurements of ice thickness and subglacial topography close to the grounding line will improve our
96   understanding of ice dynamics along the English Coast, and enable more accurate modelling of current conditions,
97   and forward-looking estimations.
98
99   **3 Methods**
100   Data sets outlined in subsections 3.1 – 3.3 are freely available to download. Download links are provided in Sect.7.
101
102   **3.1 Airborne radio echo sounding acquisition, processing, and visualisation**
103   In the austral summer of 2016/2017, the British Antarctic Survey Polarimetric-radar Airborne Science Instrument
104   (PASIN2) ice sounding radar system was used to acquire ~3,000 line km of radio-echo sounding (RES) data along
105   the English Coast of western Palmer Land, at ~3 – 5 km line spacing (Corr and Robinson, 2020). PASIN2 operates
106   at a frequency of 150 MHz, using a pulse-coded waveform at an effective acquisition rate of 312.5 Hz and a
107   bandwidth of 13 MHz. Technical details of the RES system are available in Jeofry et al. (2018) and references
108   therein. Differential GPS was used to record aircraft position (with an accuracy better than ± 1 m) and RES data
109   were collected at an average flying velocity of 55 m s^{-1}. Along-track processing of the data results in an output
110   data rate of 5 Hz, which produces an average spacing between radar traces of 11 m.

112 For the processing of the data, a coherent moving-average filter, commonly referred to as an unfocused SAR, was

113 used on the range compressed data. The onset of the bed reflector was first automatically picked using first-break

114 picker of the ProMAX seismic processing software with all picks then checked afterwards and corrected by hand

115 if necessary. The delay time of the bed reflector picks were covered to range using a standard electromagnetic

116 wave propagation speed in ice of 0.168 m ns^{-1} and a correction of 10 m to account for the near-surface high-

117 velocity firn layer (Dowdeswell and Evans 2004; Vaughan et al., 2006). Ice thickness was calculated by

118 subtracting surface elevation measurements (derived from radar/laser altimeters for aircraft terrain clearance) from

119 bed reflector depth picks. Internal crossover analysis (measurements of ice thickness at the same position) yield a

120 standard deviation of 13 m at line intersections, with no systematic line-to line biases. Independent crossover

121 analysis, with NASA's airborne Operation Ice Bridge (OIB) radar data (collected from November 2010 –

122 November 2016), yields a higher standard deviation of 75 m. Whilst this value is similar to recent independent

123 crossover analysis in other surveys, like the Pensacola-Pole basin in East Antarctica (where Paxman et al. (2019)

124 reported a standard deviation of 57.7 m), we note that our standard deviation is skewed by a number of high

125 elevation OIB flights and a relatively small number of high crossover misfits over steep subglacial topography,

126 where the bed elevation is more difficult to determine. As such, we use the internal crossover analysis value of 13

127 m for our RES errors.

129 RES transects were visualised in 2D in Reflexw radar processing software (version 7.2.2; Sandmeier Scientific

130 Software) where an energy decay gain was applied to compensate for geometric spreading losses in the radargram

131 (Daniels et al., 2004). Opendtect seismic interpretation software (2015) was employed to plot radargrams in real

132 space using DGPS co-ordinates, to enable three-dimensional analysis of RES data.

3.2 Mapping subglacial topography and ice thickness

135 Airborne RES data presented in this paper have been incorporated in the new BedMachine dataset; a self-

136 consistent dataset of the Antarctic Ice Sheet based on conservation of mass, which has a resolution of 500 m

137 (Morlighem, 2019; Morlighem et al., 2019). As a result, data presented in this paper has already been combined

138 with numerous other RES survey data (including OIB data) to produce continent-wide ice thickness and subglacial

139 topography maps (Fig. 2b). Whilst Morlighem et al. (2019) report potential vertical errors of ~100 m in central

140 Palmer Land, these values decrease towards the coast, where RES measurements are more frequent (Morlighem,

141 2019).

3.3 Surface flow speeds

144 Surface flow speeds are extracted from MEaSUREs phase-based Antarctica ice velocity map which has a

145 resolution of 450 m (Mouginot et al., 2019) (Fig. 1a). This data set combines interferometric phases from multiple

146 satellite interferometric synthetic-aperture radar systems, with additional data, including tracking-derived velocity

147 to maximise coverage from 1996 to 2018. Across western Palmer Land the average flow speed error is estimated

148 to be > 4 m a^{-1}.

3.4 Calculating ice flux

151 Using surface flow speeds (Mouginot et al., 2019), and the high-resolution ice thickness measurements along our
152 RES transects, we calculate ice flux across fixed gates delineated for each of the named ice streams and glaciers
153 along the English Coast (Fig. 2). These flux gates are delineated along RES transects close to the grounding line
154 and they span the width of each outlet. Ice flux (q) for each ice stream or glacier (j) is calculated following Eq.
155 (1):

156

157 $$q_j = \sum_{i=1}^{n} h_{ij} w_{ij} \vec{v}_{ij} \rho \tag{1}$$

158

159 where i is an equally spaced bin along the length of the flux gate, w is the bin width (which is fixed to 1 m for all
160 outlets, and is sufficiently small that the solution is not sensitive to a bin width smaller than this), $\vec{v}$ is the velocity
161 normal to the flux gate, and $\rho = 916.7$ kg m^{-3} is ice density. For simplicity, we are assuming that surface velocities
162 and ice density are constant with depth. To examine the impact of incorporating high resolution RES data into
163 gridded bed topography datasets we directly compare ice flux from Bedmap2 (Fretwell et al., 2013) (which has a
164 resolution of 1 km) with the radar picks described in Section 3.1, which are included in BedMachine (Morlighem,
165 2019) (Figure 2c). For these calculations we use the same flux gates, phase-based ice velocities and ice density;
166 simply replacing RES ice thickness for Bedmap2 ice thickness. Using available errors in velocity and ice thickness
167 datasets we calculate errors in our calculated ice flux (σ_q) for each glacier following Eq. (2):

168

169 $$\sigma_q = \sqrt{\sigma_v^2 + \sigma_h^2} \tag{2}$$

170

171 where $\sigma_v = \sum_{i=1}^{n} h_{ij} w_{ij} d\vec{v}_{ij} \rho$ and $\sigma_h = \sum_{i=1}^{n} dh_{ij} w_{ij} \vec{v}_{ij} \rho$ are the contribution of errors in velocity (dv) and ice
172 thickness (dh) to the errors in ice flux respectively. Ice flux and associated error bars for each outlet are shown in
173 Figure 2c.

174

175 **4 Results**
176 Our airborne RES transects map subglacial topography and ice thickness down the English Coast, from Ers Ice
177 Stream to Landsat Ice Stream. Whilst our results and discussion focus on the largest outlets, ice flux from each of
178 the named outlets is presented in Figure 2. The complete RES dataset (marked in Fig. 1) is freely available to
179 download from the UK Polar Data Centre (see Sect.7 for more details).

180

181 **4.1 Ers Ice Stream**
182 Close to the grounding line, Ers Ice Stream reaches a maximum flow speed of just over 940 m a^{-1} (averaging out
183 at ~2.5 m per day) (Mouginot et al., 2019). This ice originates from central Palmer Land (Fig. 1), where ice flows
184 across the west of the Antarctic Peninsula, towards Ers Ice Stream. In the upper catchment, flow speeds of ~400
185 m a^{-1} (Mouginot et al., 2019) are recorded along RES transect Ers 6 (Fig 3a). A succession of airborne RES
186 transects in Figure 3c show how this fast-flowing ice is channelised towards the coast, through a subglacial
187 depression ~8 – 14 km wide. As ice flows through this channel, towards the local grounding line (marked in white
188 on Fig. 3a), ice thickness reduces from a maximum of ~1400 m (along transect Ers 6) to between 580 and 610 m
189 (along transect Ers 1), where the ice flow is grounded ~400 m below sea level. Ice flux calculated along this radar
190 transect suggests that Ers Ice Stream contributes over 7.2 ± 0.15 Gt a^{-1} to George VI Ice Shelf (Fig. 2c). Although

191 this flux gate represents the main trunk of Ers Ice Stream (Fig 2a, 2b), neighbouring ice flow from the lateral

192 margins of the ice stream (where ice flows at ~210 – 390 m a^{-1}) will, of course, add to this value.

193

194 **4.2 Cryosat Ice Stream**

195 A central flow unit, more than 14 km wide, distinguishes Cryosat Ice Stream from neighbouring regions of slower

196 flowing ice along the English Coast (Fig. 1). Whilst surrounding ice flows at ~100 m a^{-1}, flow speeds in the ice

197 stream range from 400-500 m a^{-1} inland (along RES transect Cryosat 3), to 950 m a^{-1} (~2.6 m per day) (Mouginot

198 et al., 2019) along RES transect Cryosat 1 - which was traversed close to the Antarctic Surface Accumulation and

199 Ice Discharge (ASAID) grounding line (Bindschadler et al., 2011) (Fig. 4a). Figure 4a shows how the main flow

200 of Cryosat Ice Stream is joined by a smaller tributary to the south, where ice flow speeds increase from 180 m a^{-}

201 ^{1} along transect Cryosat 4 to over 400 m a^{-1} (Mouginot et al., 2019) along transect Cryosat 1 (traversed ~5 km

202 from the ASAID grounding line). In both flow units, the subglacial bed remains well below sea level along the

203 length of each transect. Close the grounding line, along transect Cryosat 1, the glacial bed is between 450 and 800

204 m below sea level, where overlying ice is 500 – 900 m thick. Although subglacial topographic depressions are

205 visible in-land (where subglacial peaks which reach over 500 m from the bed help to define the low elevation

206 topography), subglacial troughs become more defined towards the coast, where ice is guided through several

207 almost U-shaped troughs (Fig. 4b). This is most obvious in RES transect Cryosat 1, where the main flow of ice is

208 channelled through a ~14 km wide, 300 m deep subglacial trough close to the local grounding line, whilst the

209 smaller (southern) tributary flow is directed through a ~400 m deep trough, which is ~3 km wide at its base (Fig.

210 4b). The flow units of Cryosat Ice Stream collectively discharge just under 6 ± 0.14 Gt a^{-1} of ice across the

211 grounding line. The ice flux profile in Fig. 4b shows how much of this flux is discharged through the deep and

212 fast flowing central sector of the ice stream, rather than the deeper southern tributary.

213

214 **4.3 Sentinel Ice Stream**

215 In the MEaSUREs velocity map, Sentinel Ice Stream appears to have the widest outflow of the English Coast,

216 reaching a width of over 20 km. The main trunk of the ice stream curves round from an almost southerly flow

217 direction, to a more westerly direction along its length (Fig. 4c) as ice flow speeds increase from ~350 m a^{-1} (along

218 RES transect Sentinel 5) to ~800 m a^{-1} (closer to the grounding zone, along transect Sentinel 1) (Mouginot et al.,

219 2019). Whilst the subglacial bed remains well below sea level in all transects (at elevations in the region of -500

220 to -680 m), fluctuations in subglacial topography and ice thickness are recorded along and down flow in successive

221 RES transects (Fig. 4d). The largely unconfined ice flow in transect Sentinel 5 becomes more confined down flow

222 due to the emergence of higher elevation subglacial topography along the lateral margins of Sentinel Ice Stream.

223 These subsurface conditions are concurrent with ice thickness measurements (where maximum ice thickness

224 decreases down flow, from ~1200 m in transect Sentinel 5 to ~550 m in Sentinel 1), as well as surface velocity

225 measurements, which reveal increasing flow speeds in the central trunk of Sentinel Ice Stream with distance down

226 flow. The total flux of Sentinel Ice Stream is 6 ± 0.14 Gt a^{-1}. Whilst this flux will be added to by flow from the

227 south (where enhanced flow speeds are recorded, but they are ~3 x slower than the central trunk of Sentinel Ice

228 Stream), there will be much less flux in the north, where ice flows at a few 10s of metres per year (Mouginot et

229 al., 2019) (Fig. 4c), over higher elevation subglacial topography (~400 m higher than the base of the subglacial

230 trough).

231

4.4 Hall Glacier

233 Hall Glacier is the most northern tributary flow of the Stange Ice Shelf (Fig. 1). Surface flow speeds increase from
234 RES transect HNL 6 (close to the onset of streaming flow) - where ice flows just over 100 m a^{-1}, to RES transect
235 HNL 1 (~1.5 – 9.5 km from the ASAID grounding line and 14 km from HNL 6), where ice flow speeds reach 380
236 m a^{-1} (Mouginot et al., 2019) (Fig. 5a). These enhanced flow speeds clearly differentiate Hall Glacier from the
237 almost stagnant neighbouring ice flow (<10 m a^{-1}) along its lateral margins in Figure 5a. This figure shows how
238 the fast-flowing portion of the outlet glacier decreases in width from ~15 km inland to ~8 km along RES transect
239 HNL 2. This reduction in width coincides with a change in subsurface topography and ice thickness (Fig. 5c).
240 Whilst a shallow subglacial depression is apparent upstream, in RES transect HNL 5 (where the subglacial bed is
241 ~500 m below sea level and ice thickness reaches a maximum of 750 m), a much deeper channel is recorded down
242 flow, where ice up to 930 m thick is channelised through high elevation subglacial topography. The profile in
243 Figure 5b (derived from the flux gate marked on Figure 5a) shows the impact this subglacial topography and ice
244 thickness has on ice flux. Flux is greatest along the central trunk of Hall Glacier where a ~7 km wide subglacial
245 channel supports ice flow speeds of more than 350 m a^{-1} (Mouginot et al., 2019). Over the whole flux gate, Hall
246 Glacier contributes ~1.8 ± 0.04 Gt a^{-1} of ice to the Stange Ice Shelf, which drains into the Bellingshausen Sea
247 sector of the Southern Ocean.

248

4.5 Nikitin Glacier

250 Situated between Hall Glacier and Lidke Ice Stream, Nikitin Glacier maintains flow speeds in the region of 200-
251 450 m a^{-1} (Mouginot et al., 2019), as ice flow from central Palmer Land begins to stream towards the Stange Ice
252 Shelf (Fig. 5). For much of its length, Nikitin Glacier flows through a 15 km wide subglacial channel, where ice
253 thicknesses up to 1000 m flow over a glacial bed situated well below sea level (with elevations of -400 to -700
254 m). This low-elevation subglacial topography combined with thick ice flows and enhanced ice flow speeds enable
255 Nikitin Ice Stream to contribute over 2.13 ± 0.05 Gt a^{-1} of ice to the Stange Ice Shelf. Whilst it is difficult to
256 precisely define the point at which this ice begins to float in our radargrams, it is worth noting that complex and
257 highly reflective RES returns beneath Nikitin Ice Stream in transect HNL 1 suggest that the ice stream could be
258 afloat here. This finding is coincident with the positioning of the ASAID grounding line (Bindschadler et al.,
259 2011) (marked as a white line in Figure 5a), which is derived from satellite data.

260

4.6 Lidke Ice Stream

262 The MEaSUREs dataset (Mouiginot et al., 2019) presented in Figure 5a, shows how Lidke Ice Stream is fed by
263 two tributary flows which coalesce close to RES transect HNL 4, where ice begins to flow along a central trunk
264 at flow speeds in the region of 350 – 420 m a^{-1} (Fig. 5a). Although Lidke Ice Stream is linked to neighbouring
265 Nikitin Ice Stream in its upper catchment, a clear separation between the two ice streams is recorded down flow,
266 where the enhanced flow units become separated by a region of almost stagnant ice (< 10 m a^{-1}). RES transects
267 in Figure 5c show how this slow-moving ice sits on top of relatively high elevation subglacial topography (with
268 elevations of -380 to -500 m). This raised topography helps to define the northern margin of Lidke Ice Stream,
269 which flows through much lower elevation subglacial topography, situated ~600 – 800 m below sea level.

270

271   In RES transects HNL 4 and HNL 5 (traversed close to the onset of streaming flow) numerous peaks and troughs

272   dominate the subglacial topography returns, resulting in spatially variable ice thickness and ice flux. However,

273   further down flow, and closer to the grounding line, subglacial topography is more subdued, with the emergence

274   of a depressed subglacial channel (reaching a maximum depth of 810 m below sea level), where ice up to 1250 m

275   thick achieves surface flow speeds in the region of 400 m a^{-1} (Mouginot et al., 2019) at the grounding zone. In a

276   flux gate along HNL3 (marked in Fig. 5a), Lidke Ice Stream is calculated to contribute >2.7 ± 0.01 Gt a^{-1} to the

277   Stange Ice Shelf. The flux profile in Figure 5b shows how this value is distributed across the glacier – with high

278   flux values recorded in areas which have low elevation subglacial topography, thicker ice, and fast ice flow.

279

280   **4.7 Landsat Ice Stream**

281   Landsat Ice Stream (situated close to the catchment-defined boundary between the Antarctic Peninsula and West

282   Antarctica) is formed of a northern and southern tributary, with ice flow converging at, or close to the ASAID

283   grounding line (Fig. 6). Both tributaries have similar characteristics: they each reach flow speeds in excess of 500

284   m a^{-1} in the centre of the ice flow (along RES transect Landsat 3) before flow begins to accelerate downstream (to

285   over 700 m a^{-1} near transect Landsat 1) (Mouginot et al., 2019). Between the two tributaries, flow speeds are much

286   lower, ranging from 40 m a^{-1} (25 km inland of the grounding line), to ~100 m a^{-1} (along RES transect Landsat 1,

287   traversed close to the local grounding line) (Mouginot et al., 2019). A sequence of airborne RES transects in

288   Figure 6c show that these flow speeds reflect subglacial topography. Both tributaries flow through deep subglacial

289   basins (situated ~700 m below sea level), where ice flows up to 900 m thick are increasingly channelised towards

290   the coast by higher subglacial topography along the ice stream's lateral margins. Along RES transect Landsat 2,

291   ice flux gates across the north and south tributary flows combine to produce a total ice flux of 7.2 ± 0.13 Gt a^{-1}.

292   Between these two flow units ice flux is substantially lower, because of lower surface flow speeds, elevated

293   subglacial topography, and reduced ice thickness.

294

295   **5 Discussion**

296   English Coast ice streams and glaciers contribute over 39.2 ± 0.79 Gt a^{-1} of ice to floating ice shelves in the

297   Bellingshausen Sea. This ice flows from the center of Palmer Land, towards the coast, where discrete ice flows

298   develop in line with, and as a result of depressed subglacial topography - in a region of Antarctica where the

299   glacial bed is situated well below sea level. In the following paragraphs, we briefly discuss the main features of

300   each major ice stream (documented in the results) from north to south. The significance of the radar data set is

301   presented in Sect. 6.

302

303   **5.1 Ers Ice Stream**

304   Ers Ice Stream, at the northern extremity of our study site, produces the largest ice flux of all English Coast ice

305   streams (Fig. 2c). This is the result of elevated surface flow speeds (Mouiginot et al., 2019), substantial ice

306   thicknesses and pronounced subglacial topography, which, for the most part, channelises ice through a wide

307   subglacial depression (Fig. 3c). Enhanced ice flow is also recorded on either side of the subglacial channel, where

308   surface flow speeds >100 m a^{-1} (Mouiginot et al., 2019) contribute over ~100,000 tonnes of ice to George VI Ice

309   Shelf per year. This enhanced ice flow makes it difficult to precisely map the lateral margins of the ice stream and

310   fully assess the individual contribution of Ers Ice Stream to English Coast ice flux. However, it is clear that this

311   area of the English Coast contributes substantial and continued ice flux to George VI Ice Shelf, as a result of high

312   surface flow speeds, thick ice and deep subglacial topography.

313

314   **5.2 Cryosat Ice Stream**

315   Although ice flux from Cryosat Ice Stream is >50% lower than neighbouring Ers Ice Stream, it boasts the greatest

316   surface flow speeds of the English Coast: flowing at a maximum of 950 m a^{-1} (Mouiginot et al., 2019) (averaging

317   out at >2.6 m per day). These enhanced ice flow speeds are recorded along the width of the ice stream, where

318   thick ice flows through, and over multiple, deep incisions in the basal topography (Fig. 4b). Fig. 4a shows how

319   these ice flow speeds are maintained across the grounding zone, as ice flows into George VI Ice Shelf. As the ice

320   shelf buttresses the inland ice flow of Cryosat Ice Stream, further thinning of the ice shelf could reduce resistive

321   stress (buttressing) at the grounding line, subsequently increasing ice discharge in this region (Tsai et al., 2015;

322   Minchew et al., 2018).

323

324   **5.3 Sentinel Ice Stream**

325   Pronounced topographic depressions in most of the cross-flow radar lines that transect Sentinel Ice Stream (Fig.

326   4d) suggest a degree of topographic confinement for Sentinel Ice Stream, which is grounded >500 m below sea

327   level. Whilst this confinement helps to channelise over 6 Gt a^{-1} of ice towards the local grounding line currently,

328   along-flow radargrams in Figure 7a show how the ice stream might respond to future ingress of the grounding

329   line position (e.g. Christie et al., 2016). Ice stream thickness fluctuates in conjunction with subglacial topography

330   down the main trunk of the ice stream - from the upper catchment of the ice stream to the floating ice tongue,

331   which is recorded by bright, white RES reflectors in Fig, 7a. These bright reflectors help to highlight the grounding

332   zone (MacGregor et al., 2011), where ice flexes in response to tidal modulation (e.g. Rosier and Gudmundsson,

333   2018). Annotations in Figure 7a point out a range of previously unknown subglacial features beneath Sentinel Ice

334   Stream, like reverse subglacial slopes close to the grounding zone (which decline inland at ~5.5 – 4.5 ° per km),

335   as well as more raised topographic features further inland. These measurements are critical for simulations of

336   groundling line retreat. They show that a retreat of the grounding line into deeper water could allow thicker ice to

337   reach floatation, which would increase glacier driving stress and ice flux across the grounding line (Tsai et al.,

338   2015), with immediate implications for ice flow speed, ice discharge, and meltwater contribution to the Southern

339   Ocean (Minchew et al., 2018). RES measurements inland of the present-day grounding line reveal a steep reverse

340   bed-slope, which after an initial retreat of the grounding line (due to some forcing) could promote unstable

341   (runaway) grounding retreat (e.g. Schoof 2007; Jamieson et al., 2012; Kleman and Applegate, 2014). However,

342   elevated subglacial topography ~10 km inland of the current grounding line could potentially act as a pinning

343   point for future ice stream re-grounding (Favier et al., 2016) (Fig, 7a). Our RES measurements will allow these

344   potential instabilities to be explored in new, high-resolution numerical modelling simulations.

345

346   **5.4 Hall Glacier, Nikitin Glacier and Lidke Ice Stream**

347   Further down the English Coast, Hall Glacier, Nikitin Glacier and Lidke Ice Stream are clearly discernible in

348   maps of surface ice flow speeds (Mouiginot et al., 2019) (Fig. 1) and subsurface topography maps, like Bedmap2

349   (Fretwell et al., 2013) and the newer, higher resolution BedMachine (Morlighem et al., 2019) (Fig. 2). These maps

350   show how discrete ice flow units develop in accordance with subglacial depressions, where elevated subglacial

351 topography between tributaries help to promote independent, channelised ice flow towards the coast (Fig. 5). All

352 three ice flows converge in the floating Stange Ice Shelf, where they release a combined ice flux of ~6.7 Gt a^{-1}.

353 The zone between grounded and floating ice is discernible in satellite data (Bindschadler et al., 2011) (noted by

354 the ASAID grounding line in Figure 5a) and in our RES dataset, where bright subglacial reflections suggest water

355 ingress (MacGregor et al., 2011) along line HNL 1 (Fig.5). These independent data sets mark the same grounding

356 zone position along the English Coast. Whilst our radargrams do not extend seaward of transect HNL 1, we

357 hypothesise that the 8 km digression of the ASAID grounding line in Figure 5a could reflect the subglacial

358 extension of the deep subglacial trough beneath Hall Glacier. This relative extension of the grounding line shows

359 the impact subglacial troughs can have on grounding line location and potentially grounding line stability (as

360 noted in other regions of Antarctica, by Jamieson et al. (2012)). Should the grounding line migrate in the future,

361 relatively small-scale subsurface features like these could result in substantially different reactions from

362 neighbouring ice flows, like Hall Glacier, Nikitin Glacier and Lidke Ice Stream.

363

364 **5.5 Landsat Ice Stream**

365 The final radar transects in our survey were flown across Landsat Ice Stream (Fig. 6). These radargrams reveal

366 topographically confined ice flow along two discrete tributaries (north and south) for more than 15 km. These ice

367 streams, which flow at speeds >500 m a^{-1} (Mouiginot et al., 2019) contribute over 7.2 Gt a^{-1} of ice to the

368 Bellingshausen Sea. Along-flow lines presented in Figure 7b show the differences in ice thickness and subglacial

369 topography between the north and south tributaries of Landsat Ice Stream, which are each grounded >700 m below

370 sea level. The north tributary flows across a remarkably flat bed for most of its length, but this is punctuated by a

371 region of elevated subglacial topography ~5 km inland of the current grounding line, which is ~100 m higher than

372 surrounding bed returns (Landsat 6 transect, Fig. 7b). Whilst this generally flat, low-elevation subglacial bed

373 could enable rapid grounding line retreat in response to mass balance changes and/or applied oceanic forcings

374 (Weertman, 1974; Jamieson et al., 2012), this region of elevated subglacial topography could act as a temporary

375 pinning point for re-grounding in a retreating ice sheet scenario. A similar potential pinning point is located much

376 further inland of the grounding zone on the south tributary of Landsat Glacier (RES transect Landsat 7, Fig. 7b).

377 Here, flat subglacial topography (situated ~600 m below sea level) extends ~12 km inland of the current grounding

378 line, until bed topography lowers slightly and then inclines by 120 m over 2 km. Beyond this point, there is a

379 reverse slope, dipping inland at 3.5° per km. This subglacial topography correlates with satellite-derived surface

380 ice flow speeds (recorded by Mouginot et al., 2019): enhanced flow is recorded along RES transect Landsat 1,

381 where bright subglacial reflectors suggest the presence of subglacial water (MacGregor et al., 2011). These

382 reflections, which extend inland of the ASAID grounding line could provide the subglacial evidence to corroborate

383 recent satellite-derived measurements of inland grounding-line migration in this region of Antarctica (Christie et

384 al., 2016; Konrad et al., 2018). As warm circumpolar deep water resides at ~300 m depth in the neighbouring

385 ocean (Kimura et al, 2015) any relatively warm water ingress inland could promote ice dynamical imbalance in

386 this region of Antarctica and lead to further drawdown of ice from the interior (as reported by Hogg et al., 2017).

387

388 **6 Significance of the dataset**

389 Our RES data set provides the scientific community with over 3,000 km of airborne RES data along the English

390 Coast of the Antarctic Peninsula. The density of transects (at 3 – 5 km line spacing), and coverage so close to the

391   grounding line is unusual. Resultant latitude, longitude and elevation data (available from the Polar Data Centre)

392   adds considerable ice thickness and subglacial topographic information to this area of Antarctica, where pre-

393   existing and reliable ice penetrating radar data sets are more infrequent than other regions of the continent (like

394   central Graham Land or Pine Island Glacier). Figure 2c shows the impact this dataset has on ice flux estimations,

395   compared to older continent-wide compilations of ice thickness and subglacial topography. Ice flux calculated

396   using our new RES measurements yields a total ice flux 39.2 ± 0.79 Gt a^{-1}. Whist this is similar to flux derived

397   from Bedmap2 ice thickness measurements (Fretwell et al., 2013) (39.8 ± 7.1 Gt a^{-1}), high errors are associated

398   with this older dataset, and there are regional discrepancies between the ice flux measurements. Along the upper

399   stretch of the English Coast (Ers, Envisat, Cryosat, Grace and Sentinel ice streams, and Hall Glacier), Bedmap2

400   overestimates ice flux by ~ 2.6 Gt a^{-1} and along the southern outflows (Nikitin Glacier, Lidke Ice Stream and

401   Landsat Ice Stream) Bedmap2 underestimates ice flux by ~ 1.3 Gt a^{-1}, compared to our RES ice thickness

402   measurements. Due to the coarse resolution and limited number of IPR measurements incorporated in Bedmap2,

403   errors in ice thickness are on the order of 100s of metres and range from 13-45% of total ice thickness across our

404   flux gates. RES data presented here are of much higher resolution, where calculated internal errors in ice thickness

405   are < 3% of ice thickness measurements along each flux gate. Inclusion of these new IPR measurements in

406   BedMachine (Morlighem, 2019) has greatly improved the resolution and accuracy of the latest continent-wide

407   subglacial topography and ice thickness maps (Figure 2). Accurate, high resolution ice thickness and subglacial

408   bed measurements are crucial for understanding ice flow and modelling ice dynamics. It must therefore remain a

409   future research priority to collect more IPR data across the Antarctic Ice Sheet, and target regions that remain

410   geophysically understudied. These IPR measurements should be collected along- and across-flow to capture

411   small-scale topographic perturbations in the subglacial bed (e.g. Figure 7), which are critical for assessing the

412   potential for grounding line retreat and marine ice sheet instability.

413

414   **7 Data Availability**

415   Radio echo sounding data used in this paper, from Corr and Robinson (2020) are available through the UK Polar

416   Data Center: https://doi.org/10.5285/E07D62BF-D58C-4187-A019-59BE998939CC. Data related to surface ice

417   velocity from MEaSUREs (Mouginot et al., 2019) can be downloaded here: https://nsidc.org/data/NSIDC-

418   0754/versions/1. Maps of subglacial topography and ice thickness can be accessed from the BedMachine

419   repository (Morlighem, 2019): https://nsidc.org/data/nsidc-0756.

420

421   **8 Conclusions**

422   Ice penetrating radar transects along the English Coast of western Palmer Land in the Bellingshausen Sea sector

423   of the Antarctic Peninsula reveal multiple topographically confined ice flows, grounded $\sim 300 – 800$ m below sea

424   level. New ice thickness data, combined with satellite derived surface flow speeds from MEaSUREs (Mouiginot

425   et al., 2019) allow us to improve ice flux calculations along the recently named Ers, Envisat, Cryosat, Grace,

426   Sentinel and Landsat ice streams as well as the previously titled Hall and Nikitin glaciers and Lidke Ice Stream.

427   At a time when satellites are recording widespread grounding line retreat (Christie et al. 2016; Konrad et al.,

428   2018), surface lowering (attributed to glacier thinning) (Wouters et al., 2015; Hogg et al., 2017; Smith et al., 2020)

429   and significant mass loss (McMillan et al., 2014; Wouters et al., 2015; Martín-Español et al., 2016; Hogg et al.,

430   2017) along the English Coast, our radio-echo-sounding (RES) dataset provides the high resolution ice thickness,

Earth System
Science
Data
Open Access
Discussions

431 and subglacial topography data required for change detection. These measurements and analysis will improve

432 simulations of Antarctic coastal change and associated global sea level estimations.

433

434 **Author contributions**

435 All authors contributed to the writing and editing of the paper. K. Winter was the principle investigator of the

436 project, which was instigated by G. H. Gudmundsson and guided by J. Woodward. Ice flux calculations were

437 provided by E. A. Hill.

438

439 **Competing Interests**

440 The authors declare that they have no conflict of interest.

441

442 **Acknowledgements**

446

447 **References**

448 Bindschadler, R., Choi, H., Wichlacz, A., Bingham, R., Bohlander, J., Brunt, K., Corr, H. F. J.,

449   Drews, R., Fricker, H., Hall, M., Hindmarsh, R., Kohler, J., Padman, L., Rack, W., Rotschky, G.,

450   Urbini, S., Vornberger, P., and Young, N.: Getting around Antarctica: new high-resolution

451   mappings of the grounded and freely-floating boundaries of the Antarctic ice sheet created for the

452   International Polar Year, The Cryosphere, 5, 569-588, https://doi.org/10.5194/tc-5-569-2011,

453   2011.

454 Christie, F. D. W., Bingham, R., Gourmelen, N., Tett, S. F. B., and Muto, A.: Four-decade

455   record of pervasive grounding line retreat along the Bellingshausen margin of West Antarctica,

456   Geophysical Research letters, 43, 5741-5749, https://doi.org/10.1002/2016GL068972, 2016.

457 Corr, H., and Robinson, C.: Airborne radio-echo sounding of the English Coast, western Palmer Land, Antarctic

458   Peninsula (2016/17 season) (Version 1.0), UK Polar Data Centre, Natural Environment Research Council,

459   UK Research & Innovation, https://doi.org/10.5285/E07D62BF-D58C-4187-A019-59BE998939CC, 2020.

460 Daniels, D. J.: Ground penetrating radar, (2nd ed.). London: The Institute of Engineering and

461   Technology, https://doi.org/10.1049/PBRA015E, 2004.

462 Dowdeswell, J. A., and Evans, S.: Investigations of the form and flow of ice sheets and glaciers using radio

463   echo sounding, Reports on Physics, 67, https://doi.org/10.1088/0034-4885/67/10/R03, 2004.

464 Favier, L., Pattyn, F., Berger, S., and Drews, R.: Dynamic influence of pinning points on

465   marine ice-sheet stability: a numerical study in Dronning Maud Land, East Antarctica, The

466   Cryosphere, 10, 2623–2635, https://doi.org/10.5194/tc-10-2623-2016, 2016.

467 Fretwell, P., et al.: Bedmap2: Improved ice bed, surface and thickness datasets for Antarctica,

468   Cryosphere, 7, 375–393, https://doi.org/10.5194/tc-7-375-2013, 2013.

469 Fürst, J. J., Durand, G., Gillet-Chaulet, F., Tavard, L., Rankl, M., Braun, M., and Gagliardini, O.: The

470   safety band of Antarctic ice shelves, Nature Climate Change, 6(5), 479–482,

471   https://doi.org/10.1038/NCLIMATE2912, 2016.

472   Gudmundsson, G. H., Krug, J., Durand, G., Favier, L., and Gagliardini, O.: The stability of

473   grounding lines on retrograde slopes, Cryosphere, 6, 1497–1505, https://doi.org/10.5194/tc-6

474   -1497-2012, 2012.

475   Gudmundsson, G. H.: Ice-shelf buttressing and the stability of marine ice sheets, The

476   Cryosphere, 7, 647–655, https://doi.org/10.5194/tc-7-647-2013, 2013.

477   Helm, V., Humbert, A., and Miller, H.: Elevation and elevation change of Greenland and

478   Antarctica derived from CryoSat-2, Cryosphere, 8, 1539–1559, https://doi.org/10.5194/tc-8-1539

479   2014, 2014.

480   Hogg, A. E., Shepherd, A., Cornford, S. L., Briggs, K. H., Gourmelen, N., Graham, J. A., Joughin, I.,

481   Mouginot, J., Nagler, T., Payne, A. J., Rignot, E., and Wuite, J.: Increased ice flow in

482   Western Palmer Land linked to ocean melting, Geophysical Research Letters, 44, 4159-4167,

483   https://doi.org/10.1002/2016GL072110, 2017.

484   Jamieson, S. S. R., Vieli, A., Livingstone, S. J., Cofaigh, C. O., Stokes, C., Hillenbrand, C.-D., and

485   Dowdeswell, J. A.: Ice-stream stability on a reverse bed slope, Nature Geoscience, 5, 799

486   802, https://doi.org/doi:10.1038/ngeo1600, 2012.

487   Jeofry, H., Ross, N., Corr, H. F. J., Li, J., Gogineni, P., and Siegert, M. J.: A new bed elevation

488   model for the Weddell Sea sector of the West Antarctic Ice Sheet. Earth System Science Data, 10,

489   1– 21, https://doi.org/10.5194/essd-2017-90, 2018.

490   Kimura, S., Nicholls, K. W., and Venables, E.: Estimation of ice shelf melt rate in the presence of a

491   thermohaline staircase, Journal of Oceanography, 45, 133–148, https://doi.org/10.1175/JPO-D-13-0219.1.,

492   (2015).

493   Kleman, J., and Applegate, P. J.: Durations and propagation patterns of ice sheet instability

494   events, Quaternary Science Reviews, 92, 32-39, https://doi.org/10.1016/j.quascirev.2013.07.030,

495   2014.

496   Konrad, H., Shepherd, A., Gilbert, L., Hogg, A. E., McMillan, M., Muir, A., and Slater, T.:

497   Net retreat of Antarctic glacier grounding lines. Nature Geoscience, 11, 258–262,

498   https://doi.org/10.1038/s41561-018-0082-z, 2018.

499   Kowal, K. N., Pegler S. S., and Worster, M. G.; Dynamics of laterally confined marine ice

500   sheets. Journal of Fluid. Mechanics, 790(R2), 1–14, https://doi.org/10.1017/jfm.2016.37, 2016.

501   Lythe, M. B., Vaughan, D. G., and the BEDMAP Consortium; A new ice thickness and

502   subglacial topographic model of Antarctica. Journal of Geophysical Research: Solid Earth, 106

503   (B6), 11,335-11,351, https://doi.org/10.1029/2000JB900449, 2001.

504   MacGregor, J. A., Anandakrishnan, S., Catania, G. A., Winebrenner, D. P.; The grounding

505   zone of the Ross Ice Shelf, West Antarctica, from ice-penetrating radar. Journal of Glaciology, 57

506   (205), 917-928, https://doi.org/10.3189/002214311798043780, 2011.

507   Martín-Español, A., Zammit-Mangion, A., Clarke, P. J., Flament, T., Helm, V., King, M. A., Luthcke,

508   S. B., Petrie, E., Rémy, F., Schön, N., Wouters, B., and Bamber, J. L.: Spatial and temporal

509   Antarctic Ice Sheet mass trends, glacio-isostatic adjustment, and surface processes from a joint

510   inversion of satellite altimeter, gravity, and GPS data, Journal of Geophysical Research: Earth

511 Surface, 121, 182–200, https://doi.org/10.1002/2015JF003550, 2016.

512 McMillan, M, Shepherd, A. Sundal, A., Briggs, K., Muir, A. Ridout, A. Hogg, A., and Wingham, D.:

513 Increased ice losses from Antarctica detected by CryoSat-2, Geophysical Research Letters,

514 41, 3899–3905, https://doi.org/10.1002/2014GL060111, 2014.

515 Minchew, B. M., Gudmundsson, G. H., Gardner, A. S., Paolo, F. S., and Fricker, H. A.:

516 Modeling the dynamic response of outlet glaciers to observed ice shelf thinning in the

517 Bellingshausen Sea Sector, West Antarctica, Journal of Glaciology, 64(244), 333-342,

518 https://doi.org/10.1017/jog.2018.24, 2018.

519 Morlighem, M.: MEaSUREs BedMachine Antarctica, Version 1. Boulder, Colorado USA.

520 NASA National Snow and Ice Data Center Distributed Active Archive Center,

521 https://doi.org/10.5067/C2GFER6PTOS4, 2019.

522 Morlighem, M., et al.: Deep glacial troughs and stabilizing ridges unveiled beneath the

523 margins of the Antarctic ice sheet, Nature Geoscience, 13, 132-137,

524 https://doi.org/10.1038/s41561-019-0510-8, 2019.

525 Mouginot, J., Rignot, E., and Scheuchl, B.: Continent-wide, interferometric SAR phase,

526 mapping of Antarctic ice velocity, Geophysical Research Letters, 46, 9710–9718,

527 https://doi.org/10.1029/2019GL083826, 2019.

528 Paxman, G. J. G., Jamieson, S. S. R., Ferraccioli, F., Jordan, T. A., Bentley, M. J., Ross, N., Forsberg,

529 R., Matsuoka, K., Steinhage, D., Eagles, G., and Casal, T. G.: Subglacial geology and

530 geomorphology of the Pensacola-Pole Basin, East Antarctica, Geochemistry, Geophysics,

531 Geosystems, 20, 2786-2807, https://doi.org/10.1029/2018GC008126, 2019.

532 Pritchard, H. D., Ligtenberg, S. R. M., Fricker, H. A., Vaughan, D. G., van den Broeke, M. R., and

533 Padman, L.; Antarctic ice-sheet loss driven by basal melting of ice shelves, Nature, 484,

534 502–505, https://doi.org/10.1038/nature10968, 2012.

535 Rignot, E.: Changes in West Antarctic ice stream dynamics observed with ALOS PALSAR data, Geophysical

536 Research Letters, 35, L12505, https://doi.org/10.1029/2008GL033365, 2008.

537 Rignot, E., Mouginot, J., Scheuchl, B., van den Broeke, M., van Wessem, M. J., and Morlighem, M.:

538 Four decades of Antarctic Ice Sheet mass balance from 1979-2017, Proceedings of the

539 National Academy of Sciences, 116(4), 1095-1103, https://doi.org/10.1073/pnas.1812883116,

540 2019.

541 Rosier, S. H. R., and Gudmundsson, G. H.: Tidal bending of ice shelves as a mechanism for

542 large-scale temporal variations in ice flow, The Cryosphere, 12(5), 1699-1713,

543 https://doi.org/10.5194/tc-12-1699-2018, 2018.

544 Schoof, C.: Ice sheet grounding line dynamics: steady states, stability and hysteresis, Journal

545 of Geophysical Research, 112, F03S28, https://doi.org/10.1029/2006JF000664, 2007.

546 Shepherd, A., Wingham, D., Mansley, J. A., D.: Inland thinning of the Amundsen Sea sector, West Antarctica,

547 Geophysical Research Letters, 29(10), 1364, https://doi.org/10.1029/2001GL014183, 2002.

548 Smith, B, and 14 others.: Pervasive ice sheet mass loss reflects competing ocean and

549 atmosphere processes, Science, https://doi.org/10.1126/science.aaz5845, 2020.

550 Tsai, V. C., Stewart, A. L., and Thompson, A. F.: Marine ice-sheet profiles and stability under

551   coulomb basal conditions, Journal of Glaciology, 61 (226), 205-215,

552   https://doi.org/10.3189/2015JoG14J221, 2015.

553   van Wessem, J. M., and 13 others: Improved representation of East Antarctic surface mass

554   balance in a regional atmospheric climate model, Journal of Glaciology, 60 (222), 761-770,

555   https://doi.org/10.3189/2014JoG14J051, 2014.

556   van Wessem, J. M., Ligtenberg, S. R. M., Reijmer, C. H., van de Berg, W. J. van den Broeke, M. R.,

557   Barrand, N. E., Thomas, E. R., Turner, J., Wuite, J., Scambos, T. A., and van Meijgaard, E.:

558   The modelled surface mass balance of the Antarctic Peninsula at 5.5 km horizontal resolution,

559   Cryosphere, 10(1), 271-285, https://doi.org/10.5194/tc-10-271-2016, 2016.

560   Vaughan, D. G., Corr, H. F. J., Ferraccioli, F., Frearson, N., O'Hare, A., Mach, D., Holt, J. W., Blankenship, D.

561   D., Morse, D. L., and Young, D. A.: New boundary conditions for the West Antarctic ice sheet: Subglacial

562   topography beneath Pine Island Glacier, Geophysical Research Letters, 330, 2–5,

563   https://doi.org/10.1029/2005GL025588, 2006.

564   Weertman, J.: Stability of the junction of an ice sheet and ice shelf, Journal of Glaciology, 13

565   (67), 3-11, https://doi.org/10.3189/S0022143000023327, 1974.

566   Wouters, B., Martin-Español, A., Helm, V., Flament, T., van Wessem, J. M., Ligtenberg, S. R. M.,

567   van den Broeke, M. R., and Bamber, J. L.: Dynamic thinning of glaciers on the Southern

568   Antarctic Peninsula, Science, 348, 899–903, https://doi.org/10.1126/science.aaa5727, 2015.
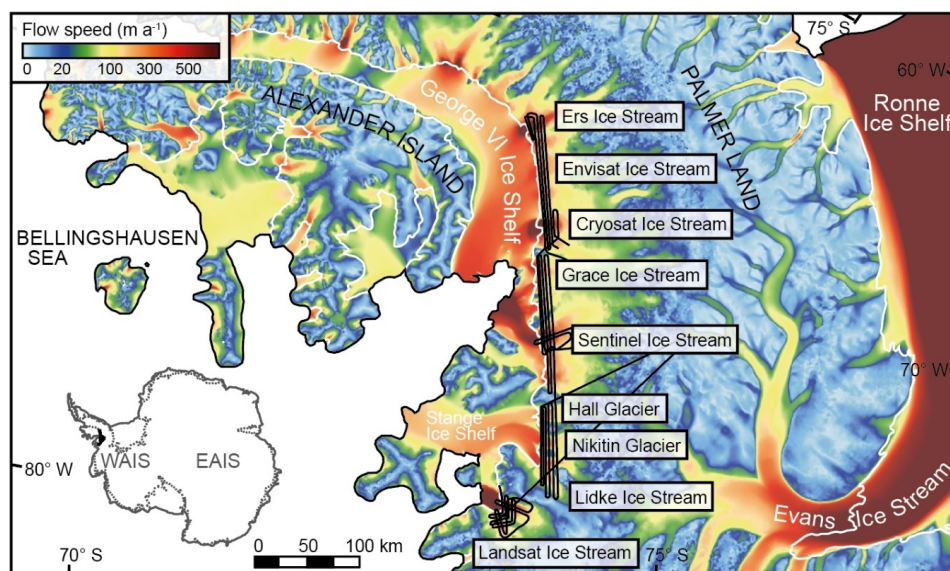
569
570
571 **Figure 1.** Airborne radio-echo sounding surveys (RES) (black lines), collected during the austral summer of
572 2016/2017, transcend the Bellingshausen Sea sector of Palmer Land in the Antarctic Peninsula. RES surveys
573 transect several glaciers and ice streams along the English Coast at, or close to the Antarctic Surface Accumulation
574 and Ice Discharge (ASAID) grounding line (white line) (Bindschadler et al., 2011), after which the ice floats.
575 Background imagery shows surface flow speeds from MEaSUREs (Mouginot et al., 2019). The inset map shows
576 the location of RES surveys used in this paper, superimposed on a map of Antarctica.
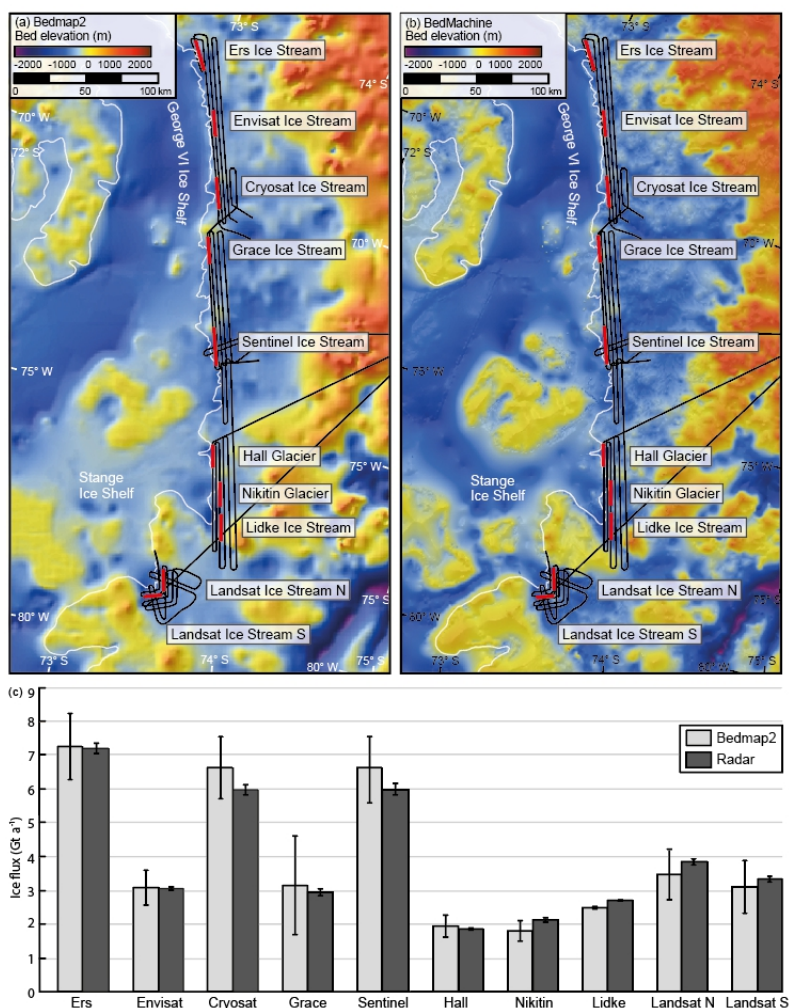
Figure 2. Major outlet glacier and ice stream flux gates (red) along the English Coast of Palmer Land. Subglacial topography maps from Bedmap2 (Fretwell et al., 2013) and BedMachine (Morlighem, 2019) are presented in panels (a) and (b). Black lines denote airborne RES transects detailed in this paper, whilst the white line shows the location of the ASAID grounding line (Bindschadler et al., 2011). Both maps show that subglacial topography frequently rests well below sea level along the English Coast. Panel (c) compares ice flux measurements (in gigatons), derived from Bedmap2 ice thickness data (Fretwell et al., 2013) (light grey bars) and direct radar measurements (dark grey bars), used as an input to BedMachine (Morlighem, 2019). These calculations utilise the same flux gates, noted in (a) and (b).
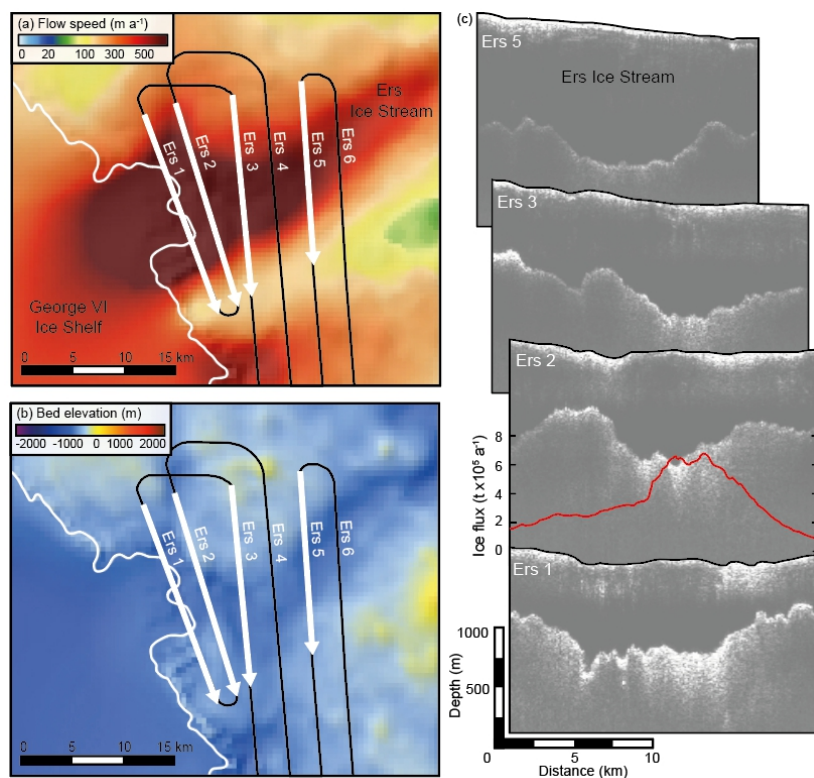
Figure 3. Ice penetrating radar transects (black lines) across Ers Glacier, superimposed on a map of surface flow speeds (Mouginot et al., 2019) (a) and subglacial topography from BedMachine (Morlighem, 2019) (b). White arrows indicate the location and direction of radargrams presented in (c) whilst the white line indicates the ASAID grounding line (Bindschadler et al., 2011). Ice flux across RES transect Ers 2 is displayed as a red line in (c). Note that the scale is in tonnes x10[5]. c) Radargrams reveal surface topography, ice thickness and the subglacial bed (recorded as diffuse white reflectors).
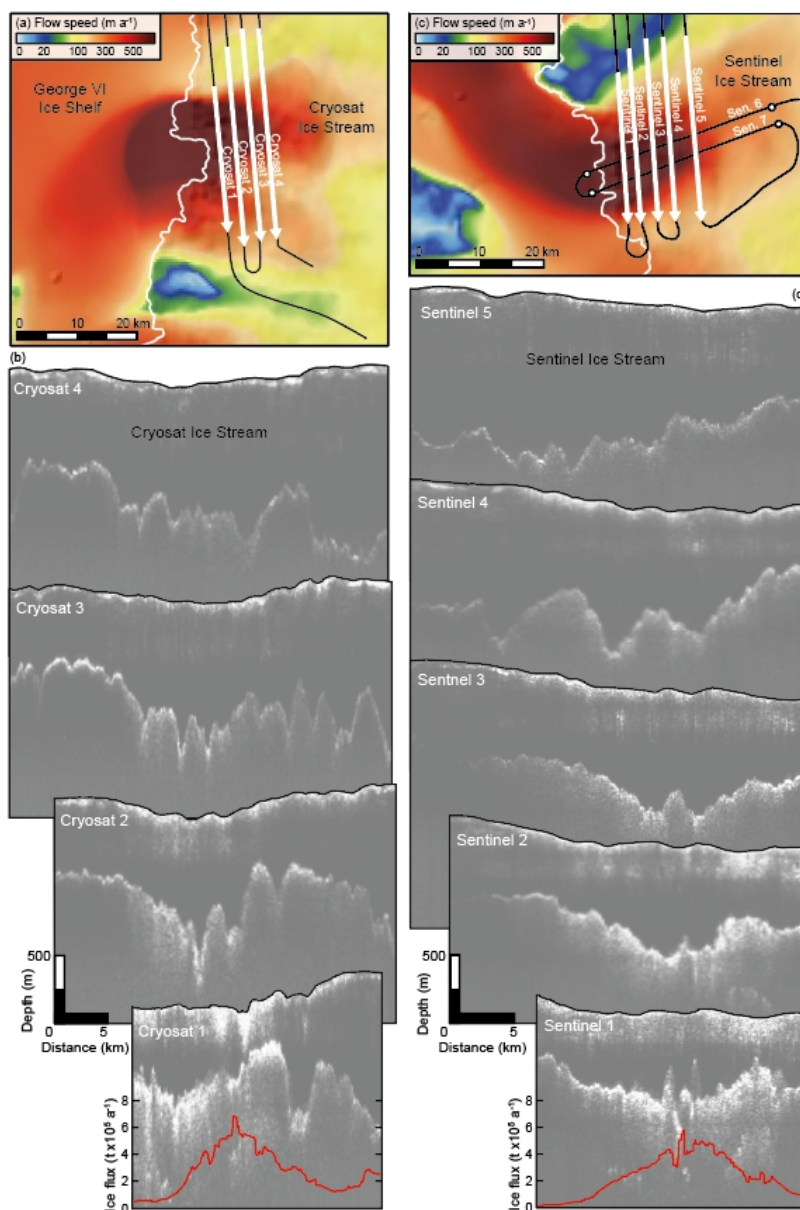
595

596

597 **Figure 4.** Radar investigations of Cryosat and Sentinel ice streams. Surface flow speed maps (Mouginot et al.,

598 2019) reveal the spatial variability in flow in panels (a) and (c). These panels highlight the location of radargrams

599 collected along the English Coast (black lines) as well as the direction and location of radargrams (white arrows)

600 displayed in (b) and (d). White lines indicate the ASAID grounding line (Bindschadler et al., 2011) whilst white

601 circles in (c) represent the extent of along-flow radar transects presented in Figure 7. Red lines in b) and d) show

602 calculated ice flux along RES transects Cryosat 1 and Sentinel 1.
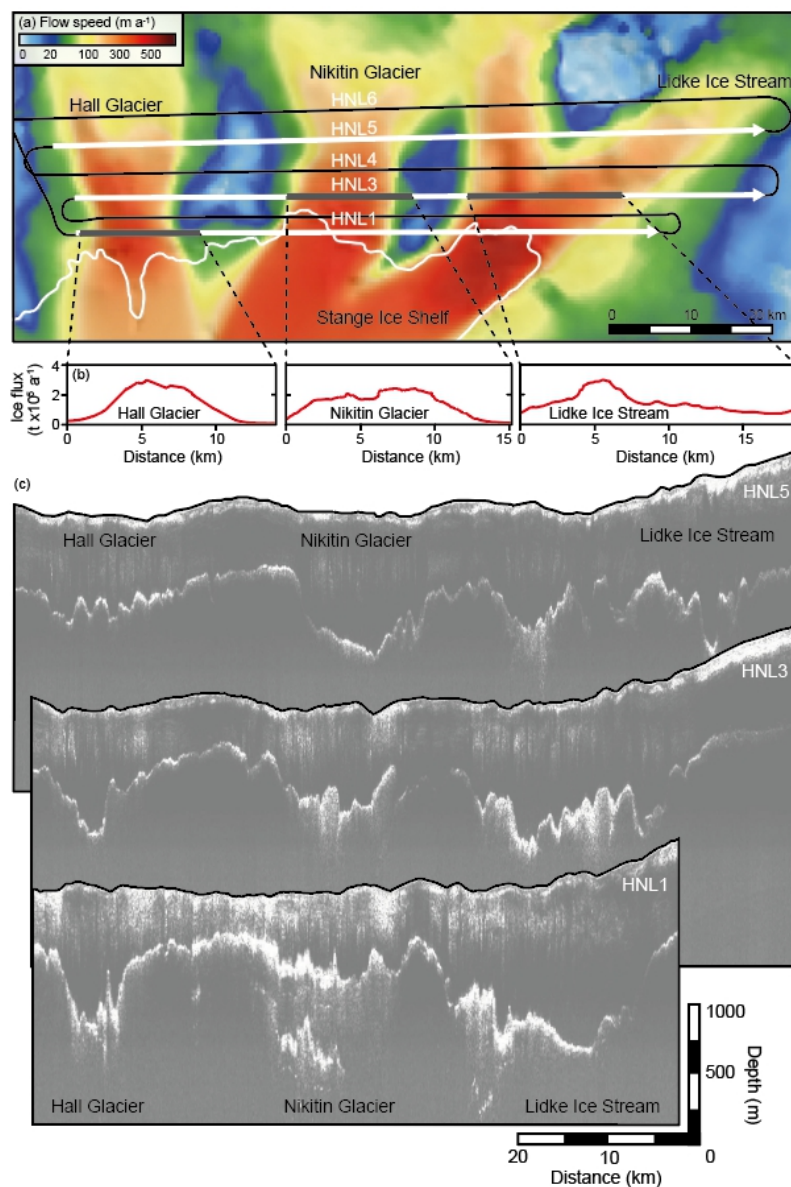
Figure 5. Hall Glacier, Nikitin Glacier and Lidke Ice Stream transfer fast flowing ice to the local grounding line (white), where ice flow coalesces in the Stange Ice Shelf. (a) surface flow speeds from Mouiginot et al. (2019), superimposed with English Coast radargram tracks (black), white arrows to indicate the location and direction of radargrams presented in (c), and thick grey lines to note ice flux gates, graphed in (b). The white line indicates the ASAID grounding line (Bindschadler et al., 2011). Note that the map has been rotated 90 degrees from its true orientation (shown in Figure 1). Radargrams in (c) reveal changes in ice thickness and subglacial topography down flow.

Earth System
Science
Data
Open Access
Discussions
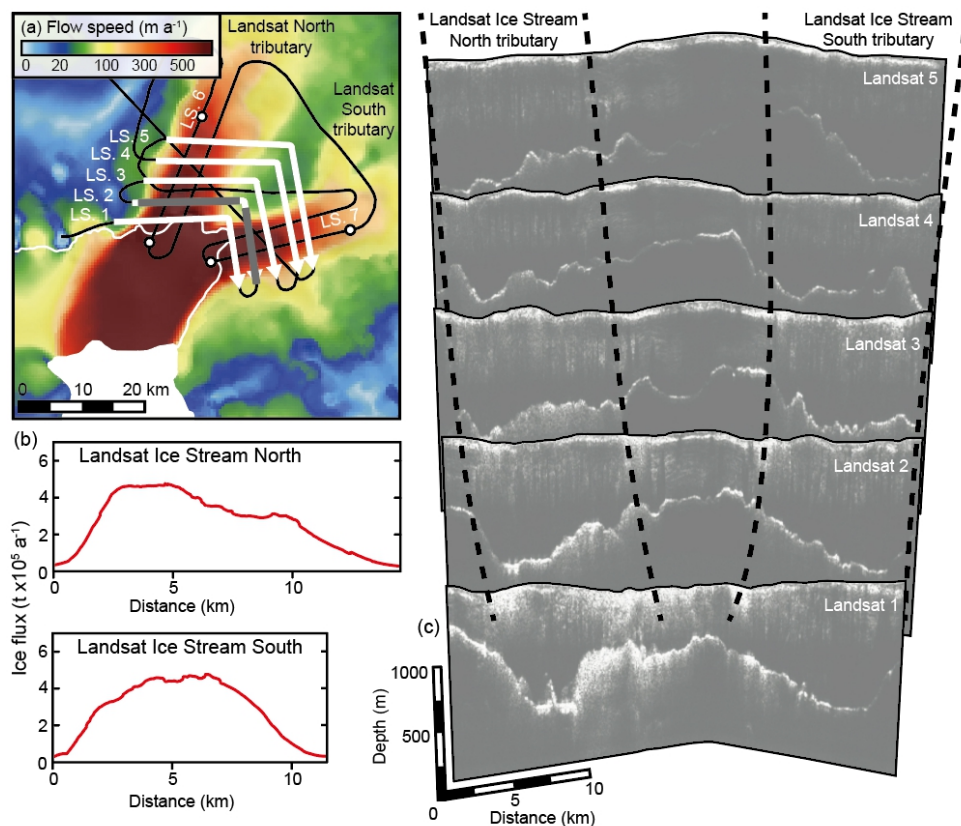
612

613

614   **Figure 6.** Landsat Ice Stream is fed by northern and southern tributaries which coalesce at the grounding zone.

615   These discrete flow units are clearly visible in (a) which shows a map of surface flow speeds from Mouginot et

616   al. (2019). Black lines show the density of RES transects in this location, whilst white arrows show the location

617   and orientation of transects displayed in (c). In panel (a) the white line represents the ASAID grounding line

618   (Bindschadler et al., 2011) whilst thick grey lines show the location of flux gates, presented in (b). White circles

619   on panel (a) represent the extent of along-flow radar transects presented in Figure 7. Radargrams in (c) show how

620   the two ice stream tributaries (approximately marked by a black dashed line) are separated by relatively high

621   elevation subglacial topography.
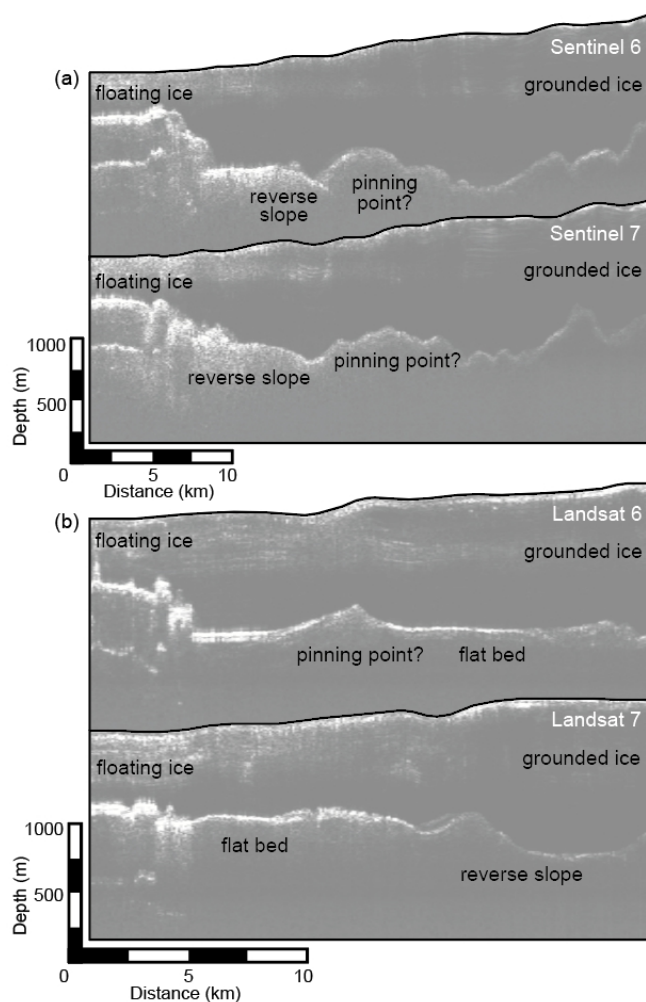
Figure 7. Along-flow radar transects of Sentinel Ice Stream (a) and Landsat Ice Stream (b). Transect locations are marked by circles in Figures 4c and 6a. All four radargrams reveal a general pattern of surface lowering and ice sheet thinning down flow (from right to left). Bright, white, diffuse reflectors on the left-hand side of the radargrams represent floating ice and water ingress. Annotations highlight these features, and basal conditions.